Journal of Computational and Applied Mathematics 303 (2016) 189–205

Contents lists available at ScienceDirect

Journal of Computational and Applied Mathematics

journal homepage: www.elsevier.com/locate/cam

An optimal cascadic multigrid method for the radiative transfer equation

Qiwei Sheng [a], Cheng Wang [b], Weimin Han [c,*]

[a] Department of Mathematics, The University of Tennessee, Knoxville, TN 37996, United States
[b] Department of Mathematics, Tongji University, Shanghai 200092, China
[c] Department of Mathematics, University of Iowa, Iowa City, IA 52242, United States

ARTICLE INFO

Article history:
Received 15 April 2015
Received in revised form 21 February 2016

MSC:
65N30
65R20

Keywords:
Radiative transfer equation
Discrete-ordinate
discontinuous-streamline diffusion
Optimal cascadic multigrid method

ABSTRACT

This paper presents a fast and optimal multigrid solver for the radiative transfer equation. A discrete-ordinate discontinuous-streamline diffusion method is employed to discretize the radiative transfer equation. Instead of utilizing conventional multigrid methods for spatial variables only, a spatial cascadic multigrid method and a full cascadic multigrid method are developed to achieve rapid convergence in iterative calculation. Preliminary analysis is also conducted, suggesting the optimal convergence rate. Numerical tests show a significant reduction of the computational time compared to conventional iterative methods for the radiative transfer equation.

1. Introduction

The radiative transfer equation (RTE), which describes the scattering and absorbing of radiation through a medium, plays an important role in a wide range of applications such as astrophysics [1], atmosphere and ocean [2–4], heat transfer [5], neutron transport and nuclear physics [6,7], and so on. Substantial research effort on the RTE began in the middle of last century. Today, research on the RTE remains to be a very active and important area, see e.g., the collections [8,9]. Recent development in biomedical engineering, such as radiotherapy dose calculations [10,11] and optical tomography [12–18], stimulates another giant wave of research in the area of radiative transfer calculations. To provide crucial information on the properties of the biological tissues, the radiative transfer cannot be ignored in a strongly spatially heterogeneous medium [19,20]. This spatial heterogeneity, on the other hand, escalates the complexity of the radiative transfer process, and results in high computational cost. Therefore, it is necessary to develop radiative transfer calculation schemes that are more suited for application to biomedical medium with a variety of tissues.

Due to the involvement of both integration and differentiation in the equation, as well as the high dimension of the problem, it is challenging to develop effective numerical schemes for solving the RTE. In the existing literature, the discretization schemes for the RTE are broadly categorized into two groups: deterministic (or explicit) and stochastic (or probabilistic). Stochastic methods [21–24] are usually employed for trajectory calculation, and are commonly considered as the golden-standard in terms of solution accuracy. However, that accuracy comes with a significant increase in both computational cost and memory requirement. In a deterministic approach, discretization of the RTE is usually carried out separately

* Corresponding author.
E-mail addresses: qsheng@utk.edu (Q. Sheng), wangcheng@tongji.edu.cn (C. Wang), weimin-han@uiowa.edu (W. Han).

http://dx.doi.org/10.1016/j.cam.2016.02.046
0377-0427/

for the spatial and angular variables. Popular spatial discretizations include finite difference methods [25], finite element methods [26,27], finite volume methods [28], and so on. Various angular discretizations exist: discrete ordinate (S_n) methods [25,29], methods using spherical harmonics (P_n methods, [6]), etc. Some earlier references on this topic include [30,25], while a few more recent references are [31–33]. It is also worth mentioning that to deal with the strongly asymmetric scattering, such as highly forward-peaked scattering, various approximations to the RTE were developed (see, e.g., [34,35] and references therein).

The choice of a particular method depends on the conditions and purposes of the radiative transfer calculation, because deterministic and stochastic approaches have their own advantages and disadvantages. One of the advantages of the deterministic approach is that it is generally capable of providing the entire spatial and angular distribution of the radiation field at once. This means that all radiative quantities, such as the intensity of radiance in an arbitrary direction, the net flux or the flux in a particular direction, can be derived from the same basic calculation result. Another advantage is that it is free of statistical noise, which is inevitable in stochastic methods due to the finite number of photons employed in practice, and therefore deterministic methods are highly competent for quantitative estimation of the effects of changes in optical parameters on the radiation distribution. However, deterministic methods still require considerable computational resources and calculation times to obtain accurate results. Therefore, it is necessary to develop fast solver for the deterministic methods satisfying the conditions of both accuracy and feasibility required in various applications.

The multigrid method (see e.g. [36,37]) has been proved to be able to efficiently accelerate convergence and thus significantly reduce the computation time. For the radiative transfer equation, D. Balsara developed and studied a full approximation scheme (FAS) incorporated with the discrete ordinate method [38]; in [39,40], a parallel spatial/angular agglomeration multigrid method employing the FAS was developed to accelerate the finite-volume method for the radiative transfer equations; in [41], both FAS and full multigrid (FMG) method were applied to the spatial and angular variables for the steady-state or frequency domain radiative transfer equation.

The purpose of this paper is to study the performance of the cascadic multigrid method (CMG) for solving the RTE. As a "one-way multigrid" method, a distinctive feature of the CMG is the total absence of coarse grid corrections, which indicates that this type of multigrid method is easier to implement than the conventional multigrid methods. The CMG is not brand new, and has been proposed and analyzed for elliptic and parabolic partial differential equations in [42–47]. However, to the best of our knowledge, the CMG has not been applied to the RTE. In the proposed CMG, the discrete-ordinate discontinuous-streamline diffusion schemes developed in [48] are employed to discretize the RTE. Both spatial CMG method and full CMG method are considered. Different from the spatial cascadic multigrid (SCMG) method that uses the same angular partition for all multigrid levels, the angular and spatial cascadic multigrid (ASCMG) method employs coarser angular partition for coarser spatial mesh while keeps the finest angular partition on the finest level, and therefore can further accelerate the computation significantly. On the other hand, since different angular partitions are employed, the ASCMG method needs an additional interpolation operator involved. Our numerical results indicate that such interpolation errors can be easily swept out by the smoothing iterations. Moreover, the numerical experiments show that the proposed CMG methods lead to a significant reduction of the computational time compared to conventional iterative methods for the radiative transfer equation, and the ASCMG method achieves a faster convergence in comparison with the SCMG method.

The rest of this paper is organized as follows: In next section, we introduce the radiative transfer equation, the relevant notation, and recall the corresponding existence and uniqueness result. In Section 3, we shall briefly review a discrete-ordinate discontinuous-streamline diffusion method for the radiative transfer equation proposed in [48]. We then present details of the CMG for the radiative transfer equation and analyze the convergence properties in Section 4. In Section 5, several numerical examples are presented to illustrate the effectiveness and convergence properties of the proposed method. Concluding comments and remarks on future work are given in Section 6.

2. Radiative transfer equation

Let X be a bounded domain in $\mathbb{R}^d$ ($d = 2, 3$) with a smooth boundary ∂X. Denote by $\boldsymbol{n}(\boldsymbol{x})$ the unit outward normal at $\boldsymbol{x} \in \partial X$. Let Ω be the angular space, i.e., the unit circle in $\mathbb{R}^2$ for $d = 2$, or the unit sphere in $\mathbb{R}^3$ for $d = 3$. For each fixed direction $\boldsymbol{\omega} \in \Omega$, we introduce the following subsets of ∂X:

$$\partial X_{\boldsymbol{\omega},-} = \{\boldsymbol{x} \in \partial X : \boldsymbol{\omega} \cdot \boldsymbol{n}(x) < 0\}, \qquad \partial X_{\boldsymbol{\omega},+} = \{\boldsymbol{x} \in \partial X : \boldsymbol{\omega} \cdot \boldsymbol{n}(x) \geq 0\}.$$

Then, we define

$$\Gamma_- = \{(\boldsymbol{x}, \boldsymbol{\omega}) : \boldsymbol{x} \in \partial X_{\boldsymbol{\omega},-}, \boldsymbol{\omega} \in \Omega\}, \qquad \Gamma_+ = \{(\boldsymbol{x}, \boldsymbol{\omega}) : \boldsymbol{x} \in \partial X_{\boldsymbol{\omega},+}, \boldsymbol{\omega} \in \Omega\}$$

as the incoming and outgoing boundaries.

Let $u(\boldsymbol{x}, \boldsymbol{\omega})$ be the radiative intensity at position $\boldsymbol{x} \in X$ along direction $\boldsymbol{\omega} \in \Omega$. We define the integral operator S by

$$(Su)(\boldsymbol{x}, \boldsymbol{\omega}) = \int_\Omega g(\boldsymbol{x}, \boldsymbol{\omega} \cdot \hat{\boldsymbol{\omega}}) u(\boldsymbol{x}, \hat{\boldsymbol{\omega}})\, d\sigma(\hat{\boldsymbol{\omega}}), \tag{1}$$

with g a non-negative phase function satisfying the normalization condition

$$\int_\Omega g(\boldsymbol{x}, \boldsymbol{\omega} \cdot \hat{\boldsymbol{\omega}})\, d\sigma(\hat{\boldsymbol{\omega}}) = 1 \quad \forall \boldsymbol{x} \in X,\ \boldsymbol{\omega} \in \Omega. \tag{2}$$

In most applications, the function g is independent of $\boldsymbol{x}$. As an example, a commonly used phase function g in the literature is the following Henyey–Greenstein (H–G) phase function [49,41]:

$$g(t) = \begin{cases} \dfrac{1-\eta^2}{2\pi(1+\eta^2-2\eta t)}, & d=2, \\ \dfrac{1-\eta^2}{4\pi(1+\eta^2-2\eta t)^{3/2}}, & d=3, \end{cases} \tag{3}$$

where the parameter $\eta \in (-1, 1)$ is the anisotropy factor of the scattering medium. Note that $\eta = 0$ for isotropic scattering, $\eta > 0$ for forward scattering, and $\eta < 0$ for backward scattering.

With the above notation, a boundary value problem of the radiative transfer equation (RTE) reads

$$\boldsymbol{\omega} \cdot \nabla u(\boldsymbol{x}, \boldsymbol{\omega}) + \sigma_t(\boldsymbol{x}) u(\boldsymbol{x}, \boldsymbol{\omega}) = \sigma_s(\boldsymbol{x})(Su)(\boldsymbol{x}, \boldsymbol{\omega}) + f(\boldsymbol{x}, \boldsymbol{\omega}), \quad (\boldsymbol{x}, \boldsymbol{\omega}) \in X \times \Omega, \tag{4}$$

$$u(\boldsymbol{x}, \boldsymbol{\omega}) = 0, \qquad (\boldsymbol{x}, \boldsymbol{\omega}) \in \Gamma_-. \tag{5}$$

Here $\sigma_t = \sigma_a + \sigma_s$, σ_a is the macroscopic absorption cross section, σ_s is the macroscopic scattering cross section, and f is a source function. We assume these given functions have the properties that

$$\sigma_t, \sigma_s \in L^\infty(X), \ \sigma_s \geq 0 \text{ a.e. in } X, \ \text{and } \sigma_t - \sigma_s \geq c_0 \text{ in } X \text{ for a constant } c_0 > 0, \tag{6}$$

$$f(\boldsymbol{x}, \boldsymbol{\omega}) \in L^2(X \times \Omega) \text{ and is continuous in } \boldsymbol{\omega} \in \Omega. \tag{7}$$

The boundary condition (5) corresponds to a physical setting of completely dark environment.

It is known (see, e.g., [50]) that under assumptions (6) and (7), the problem (4)–(5) has a unique solution $u \in H_2^1(X \times \Omega)$, where

$$H_2^1(X \times \Omega) := \{v \in L^2(X \times \Omega) : \boldsymbol{\omega} \cdot \nabla v \in L^2(X \times \Omega)\},$$

with $\boldsymbol{\omega} \cdot \nabla v$ denoting the generalized directional derivative of v in the direction $\boldsymbol{\omega}$.

3. Discrete-ordinate discontinuous-streamline diffusion method for RTE

In this section, a discrete-ordinate discontinuous-streamline diffusion method [48] is presented for solving the radiative transfer problem (4)–(5). The numerical scheme is formed in two steps. First, we use the discrete-ordinate (DO) method to approximate the integral term in the RTE, resulting in a system of linear hyperbolic equations. Then these coupled linear hyperbolic partial differential equations are discretized by the discontinuous-streamline diffusion (DSD) method.

3.1. Angular discretization

To approximate the integration term Su, we introduce a numerical quadrature of the form

$$\int_\Omega F(\boldsymbol{\omega})\, d\sigma(\boldsymbol{\omega}) \approx \sum_{l=0}^{L} w_l F(\boldsymbol{\omega}_l), \quad w_l > 0, \ \boldsymbol{\omega}_l \in \Omega, \ 0 \leq l \leq L, \tag{8}$$

where F is a continuous function over the unit sphere Ω.

3.1.1. Quadrature scheme in the two-dimensional (2D) domain

We introduce the spherical coordinates

$$\boldsymbol{\omega} = (\cos\theta, \sin\theta)^T, \quad 0 \leq \theta \leq 2\pi. \tag{9}$$

Noting that $d\sigma(\boldsymbol{\omega}) = d\theta$ for the coordinate system (9), we have

$$\int_\Omega F(\boldsymbol{\omega})\, d\sigma(\boldsymbol{\omega}) = \int_0^{2\pi} \bar{F}(\theta)\, d\theta,$$

where $\bar{F}$ stands for the representation of F in the spherical coordinates.

One possible quadrature scheme for the above integral is the composite trapezoidal formula

$$\int_0^{2\pi} \bar{F}(\theta)\, d\theta \approx \frac{h_\theta}{2}\left(\bar{F}(\theta_0) + \sum_{i=1}^{L-1} 2\bar{F}(\theta_i) + \bar{F}(\theta_L)\right) := \sum_{i=0}^{L} w_i \bar{F}(\theta_i),$$

where $L \geq 1$ is a positive integer, $\{\theta_i\}$ are evenly spaced nodes on $[0, 2\pi]$ with a spacing $h_\theta = 2\pi/L$, i.e., $\theta_i = ih_\theta$ for $0 \leq i \leq L$, and for the weights, $w_0 = w_L = \frac{h_\theta}{2}$, and $w_i = h_\theta$ for $1 \leq i \leq L-1$. It is known [51] that

$$\int_0^{2\pi} \bar{F}(\theta)\, d\theta - \frac{h_\theta}{2}\left(\bar{F}(\theta_0) + \sum_{i=1}^{L-1} 2\bar{F}(\theta_i) + \bar{F}(\theta_L)\right) = -\frac{\pi h_\theta^2}{6}\bar{F}''(\theta_c), \quad \theta_c \in [0, 2\pi]. \tag{10}$$

3.1.2. Quadrature scheme in the three-dimensional (3D) domain

We introduce the spherical coordinates

$$\boldsymbol{\omega} = (\sin\theta\cos\psi, \sin\theta\sin\psi, \cos\theta)^T, \quad 0 \le \theta \le \pi,\ 0 \le \psi \le 2\pi. \tag{11}$$

Then $d\sigma(\boldsymbol{\omega}) = \sin\theta d\theta d\psi$. By using the spherical coordinate system (11), we obtain

$$\int_\Omega F(\boldsymbol{\omega})\, d\sigma(\boldsymbol{\omega}) = \int_0^{2\pi}\int_0^{\pi} \bar{F}(\theta, \psi)\sin\theta\, d\theta d\psi.$$

One family of quadratures for the above integral is given by the product numerical integration formulas. For example, for a positive integer $m \ge 1$,

$$\int_\Omega F(\boldsymbol{\omega})\, d\sigma(\boldsymbol{\omega}) \approx \frac{\pi}{m}\sum_{j=1}^{2m}\sum_{i=1}^{m} w_i \bar{F}(\theta_i, \psi_j), \tag{12}$$

where $\{\theta_i\}$ are chosen so that $\{\cos\theta_i\}$ and $\{w_i\}$ are the Gauss–Legendre nodes and weights of m points on $[-1, 1]$. The points $\{\psi_j\}$ are evenly spaced on $[0, 2\pi]$ with a spacing of π/m. Regarding the accuracy of the quadrature (12), we have [52]

$$\left|\int_\Omega F(\boldsymbol{\omega})\, d\sigma(\boldsymbol{\omega}) - \frac{\pi}{m}\sum_{j=1}^{2m}\sum_{i=1}^{m} w_i \bar{F}(\theta_i, \psi_j)\right| \le c_s n^{-s}\|F\|_{s,\Omega} \quad \forall F \in H^s(\Omega),\ s > 1, \tag{13}$$

where c_s is a positive constant depending only on s, and n denotes the degree of precision of the quadrature. Note that for the above integration methods, we have $n = 2m - 1$.

3.1.3. Discrete-ordinate method

Based on the numerical quadratures (8), the integral operator S can be approximated by a discretization operator S_d given by

$$S_d u(\boldsymbol{x}, \boldsymbol{\omega}) = \sum_{i=0}^{L} w_i g(\boldsymbol{x}, \boldsymbol{\omega}\cdot\boldsymbol{\omega}_i) u(\boldsymbol{x}, \boldsymbol{\omega}_i). \tag{14}$$

Using the operator S_d, we can discretize the radiative transfer equation (4)–(5) in each angular direction $\boldsymbol{\omega}_l$ to get

$$\boldsymbol{\omega}_l\cdot\nabla u^l + \sigma_t u^l = \sigma_s\sum_{i=0}^{L} w_i g(\boldsymbol{x}, \boldsymbol{\omega}_l\cdot\boldsymbol{\omega}_i)u^i + f_l \quad \text{in } X,\ u^l = 0 \text{ on } \partial^l_- X,\ 0 \le l \le L, \tag{15}$$

where $f_l = f(\boldsymbol{x}, \boldsymbol{\omega}_l)$ and $u^l = u^l(\boldsymbol{x})$ is an approximation of $u(\boldsymbol{x}, \boldsymbol{\omega}_l)$. Here and below, we use the simplified notation $\partial^l_\pm X := \partial X_{\boldsymbol{\omega}_l,\pm}$.

3.2. Space discretization

The angular discretization of the RTE leads to a hyperbolic system (15) of first-order partial differential equations in space. Now we discretize (15) by use of the discontinuous-streamline diffusion method [48].

Let $\{T_h\}_h$ be a regular family of partitions of X with h the mesh size parameter. Denote by $\boldsymbol{n}_K$ the unit outward normal to ∂K for $K \in T_h$. Let E_h^i be the set of all interior boundaries (faces for $d = 3$ and edges for $d = 2$) of T_h. For any positive integer k, let $P_k(K)$ be the set of all polynomials on K of a total degree no more than k. We introduce a finite element space $V_h := \{v_h \in L^2(X) : v|_K \in P_k(K)\ \ \forall K \in T_h\}$.

For a fixed direction $\boldsymbol{\omega}_l$, we define the incoming and outgoing boundaries of $K \in T_h$ by

$$\partial^l_- K = \{\boldsymbol{x} \in \partial K : \boldsymbol{\omega}_l\cdot\boldsymbol{n}_K(\boldsymbol{x}) < 0\}, \qquad \partial^l_+ K = \{\boldsymbol{x} \in \partial K : \boldsymbol{\omega}_l\cdot\boldsymbol{n}_K(\boldsymbol{x}) \ge 0\}.$$

We remark that each edge of an element $K \in T_h$ is on either the incoming boundary or the outgoing boundary.

Let K^l_+ and K^l_- be two adjacent elements sharing $e \in E_h^i$, where the normal direction $\boldsymbol{n}^l_e$ pointing from K^l_- to K^l_+ satisfies $\boldsymbol{\omega}\cdot\boldsymbol{n}^l_e \ge 0$ (cf. Fig. 1). For a scalar-valued function v, we define

$$v^l_+ = v|_{K^l_+}, \qquad v^l_- = v|_{K^l_-}, \quad \text{and} \quad [v] = v^l_+ - v^l_- \quad \text{on } e.$$

For any domain $D \subseteq X$ with boundary ∂D (resp. $\partial^l_\pm D$), let $(\cdot,\cdot)_D$ and $\langle\cdot,\cdot\rangle_{\partial D}$ (resp. $\langle\cdot,\cdot\rangle_{\partial^l_\pm D}$) be the L^2 inner products on D and on ∂D (resp. $\partial^l_\pm D$).

Using the above notation, we define the discrete-ordinate discontinuous-streamline diffusion (DODSD) method as follows.

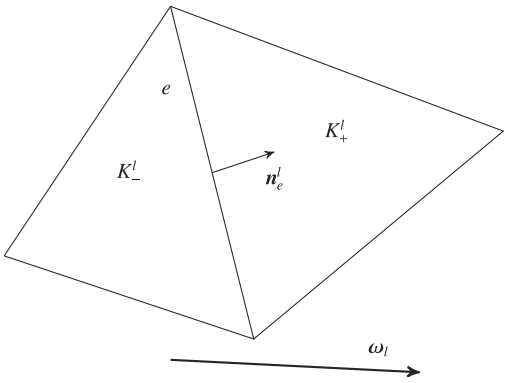

Fig. 1. An example of K_-^l, K_+^l, and $\boldsymbol{n}_e^l$ in 2D.

Find $\{u_h^l\}_{0\le l\le L} \subset (V_h)^{L+1}$ such that for any $K \in T_h$, $0 \le l \le L$,

$$\begin{aligned}&\left(\boldsymbol{\omega}_l \cdot \nabla u_h^l + \sigma_t u_h^l,\, v_h^l + \delta\, \boldsymbol{\omega}_l \cdot \nabla v_h^l\right)_K + \left\langle [u_h^l],\, v_+^l |\boldsymbol{\omega}_l \cdot \boldsymbol{n}|\right\rangle_{\partial_-^l K}\\ &\quad = \left(\sigma_s \sum_{i=0}^{L} w_i g(\boldsymbol{x}, \boldsymbol{\omega}_l \cdot \boldsymbol{\omega}_i) u_h^i + f_l,\, v_h^l + \delta\, \boldsymbol{\omega}_l \cdot \nabla v_h^l\right)_K \quad \forall\, v_h^l \in P_k(K)\end{aligned} \tag{16}$$

with

$$u_-^l = 0 \quad \text{on } \partial_-^l K \subset \partial_-^l X. \tag{17}$$

Here, $\delta = \bar{c}\, h$ is an artificial diffusion parameter with some constant $\bar{c} > 0$ and $v_\pm^l := (v_h^l)_\pm$. As is shown in [48], (16)–(17) has a unique solution.

For any $\boldsymbol{v}_h = \{v_h^l\}_{0\le l\le L} \in \boldsymbol{W}_h := \left(L^2(X)\right)^{L+1}$, define

$$\|\boldsymbol{v}_h\|_X = \left(\sum_{l=0}^{L} w_l \sum_{K\in T_h} \|v_h^l\|_{0,K}^2\right)^{\frac{1}{2}}. \tag{18}$$

For the error analysis, we make a regularity assumption:

$$\text{for some } r > 0,\ u^l \in H^{1+r}(X) \cap C(X), \quad 0 \le l \le L. \tag{19}$$

In [48], it is proved that (16)–(17) has a unique solution and the following error estimate holds.

Theorem 3.1. *Let $\{u^l\}$ and $\boldsymbol{u}_h$ be the solutions of (15) and (16)–(17), respectively. Under assumptions (6), (7), and (19), we have*

$$\left\|\{u^l\} - \boldsymbol{u}_h\right\|_X \le C h^{\min\{r,k\}+\frac{1}{2}} \left(\sum_{l=0}^{L} \|u^l\|_{r+1,X}^2\right)^{\frac{1}{2}}. \tag{20}$$

4. Cascadic multigrid method

4.1. Iteration schemes

In this subsection, we present two iteration schemes to solve the DODSD problem (16)–(17), which will be used as the smoother of the cascadic multigrid method. For simplicity, we only describe the implementation of the iteration schemes in 2D.

We first define a sequence of subsets of the set $\{K : K \in T_h\}$ with respect to a given direction $\boldsymbol{\omega}^l$ as follows, using the mesh shown in Fig. 2 for illustration.

Step 1. Denote by $T_h^{(l,1)}$ the subset of the elements for which all incoming boundary $\partial_-^l K \subset \partial_-^l X$. In Fig. 2, $T_h^{(l,1)} = \{K_i : i = 2, 3\}$.

Step 2. For $T_h \setminus T_h^{(l,1)}$, let $\partial_-^{l,1} X = \{e \subset \partial_-^l K : K \in T_h \setminus T_h^{(l,1)},\ \text{and } u_+^l|_e \text{ has been computed or given}\}$ denote its incoming edge. In Fig. 2, $\partial_-^{l,1} X$ is the broken line $\overline{ACDEF}$. Similarly, we define the subset $T_h^{(l,2)}$. In Fig. 2, $T_h^{(l,2)} = \{K_i : i = 9, 10\}$.

Step 3. Repeating step 2, we obtain the non-overlapping splitting $T_h = T_h^{(l,1)} \cup T_h^{(l,2)} \cup \cdots \cup T_h^{(l,S)}$.

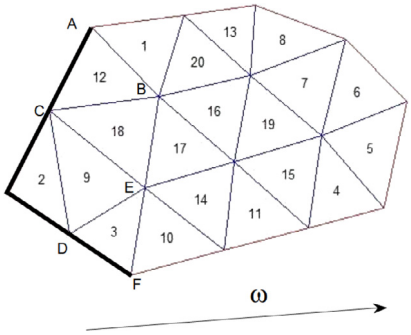

Fig. 2. A example of T_h in 2D.

4.1.1. Source iteration

Source iteration [53] is a popular method for solving the discretized linear system of RTE. In this iterative procedure, the scattering entirely lags one step behind the transport.

For each fixed direction, the transport equation can be solved efficiently by the source iteration. The computation follows the order in the subset sequence of the elements; that is, start the computation with the elements in $T_h^{(l,1)}$ and end with the elements in $T_h^{(l,S)}$. For each element $K \in T_h^{(l,s)}$, the unknown function u_h^l is computed by the following source iteration scheme of (16): find $u_h^{l,j+1} \in P_k(K)$ such that

$$\begin{aligned}&\left(\boldsymbol{\omega}_l \cdot \nabla u_h^{l,j+1} + \sigma_t u_h^{l,j+1},\, v_h^l + \delta\, \boldsymbol{\omega}_l \cdot \nabla v_h^l\right)_K + \left\langle u_+^{l,j+1},\, v_+^l |\boldsymbol{\omega}_l \cdot \boldsymbol{n}|\right\rangle_{\partial_- K}\\ &\quad = \left(\sigma_s \sum_{i=0}^{L} w_i g(\boldsymbol{x}, \boldsymbol{\omega}_l \cdot \boldsymbol{\omega}_i) u_h^{l,j} + f_l,\, v_h^l + \delta\, \boldsymbol{\omega}_l \cdot \nabla v_h^l\right)_K + \left\langle u_-^{l,j+1},\, v_+^l |\boldsymbol{\omega}_l \cdot \boldsymbol{n}|\right\rangle_{\partial_- K} \quad \forall\, v_h^l \in P_k(K) \end{aligned} \tag{21}$$

with the given $u_-^{l,j+1}|_{\partial_- K}$ and $u_h^{l,j}$. Here $u_h^{l,j}$ denotes the approximation of u_h^l obtained in the previous iteration.

We remark that $u_h^{l,j+1}$ on the elements in each $T_h^{(L,i)}$ can be computed independently. Furthermore, in 2D cases, if we use linear finite elements for the space discretization, then the coefficient matrix of the linear system generated by (21) is a 3-by-3 square matrix, the combined coefficient matrix for the computation of u_h^l on $T_h^{(i)}$ is a reducible tridiagonal matrix, and the linear system can be easily solved by the tridiagonal matrix algorithm.

The source iteration scheme can be described as follows:

Algorithm 1: Source iteration

Set parameters: tol, δ
Initialization: $\{u_h^{l,0}\} = \{0\}$, $err = tol + 1$, $j = 0$
while $err \geq tol$ **do**
  Set $\{u_h^{l,j+1}\} = \{u_h^{l,j}\}$
  Compute $S_d\left(\{u_h^{l,j}\}\right) = \sum_{i=0}^{L} w_i g(\boldsymbol{x}, \boldsymbol{\omega}_l \cdot \boldsymbol{\omega}_i) u_h^{l,j}$
  for $l = 0$ *to* L **do** % cycle for direction
    for $s = 1$ *to* S **do** % cycle for $T_h^{(l,s)}$
      Update $u_h^{l,j+1}$ on all elements K in $T_h^{(l,s)}$ by solving the problem (21)
    end for
  end for
  Compute $err = \left\| \{u_h^{l,j+1}\} - \{u_h^{l,j}\} \right\|_X$
  Set $j = j + 1$
end while

4.1.2. Gauss–Seidel (GS) iteration

The source iteration converges slowly when the scattering is dominant, e.g., in the optically thick regime where the domain size is large in terms of mean free paths. Therefore, we present a Gauss–Seidel like iteration scheme [41] in Algorithm 2. The Gauss–Seidel iteration scheme utilizes the most updated value of u_h^l, and computes the numerical approximation $S_d^{h_\theta}$ for each iteration. That is, for each element $K \in T_h^{(l,s)}$, the unknown function u_h^l is computed by the following Gauss–Seidel

iteration scheme of (16): $u_h^{l,j+1} \in P_k(K)$ such that

$$\begin{aligned}&\left(\boldsymbol{\omega}_l \cdot \nabla u_h^{l,j+1} + \sigma_t u_h^{l,j+1},\, v_h^l + \delta\, \boldsymbol{\omega}_l \cdot \nabla v_h^l\right)_K + \left\langle u_+^{l,j+1},\, v_+^l |\boldsymbol{\omega}_l \cdot \boldsymbol{n}|\right\rangle_{\partial_-^l K}\\ &= \left(\sigma_s \sum_{i=0}^{L} w_i g(\boldsymbol{x}, \boldsymbol{\omega}_l \cdot \boldsymbol{\omega}_i)\hat{u}_h^{l,j+1} + f_l,\, v_h^l + \delta\, \boldsymbol{\omega}_l \cdot \nabla v_h^l\right)_K + \left\langle u_-^{l,j+1},\, v_+^l |\boldsymbol{\omega}_l \cdot \boldsymbol{n}|\right\rangle_{\partial_-^l K} \quad \forall\, v_h^l \in P_k(K)\end{aligned} \tag{22}$$

where

$$\hat{u}_h^{l,j+1} = \begin{cases} u_h^{l,j+1} & \text{if } u_h^{l,j+1} \text{ is available,} \\ u_h^{l,j} & \text{otherwise.}\end{cases} \tag{23}$$

In Section 5, we show the improvement of the Gauss–Seidel iteration scheme by numerical tests.

Algorithm 2: Gauss–Seidel iteration

Set parameter: tol, δ
Initialization: $\{u_h^{l,0}\} = \{0\}$, $err = tol + 1$, $j = 0$
while $err \geq tol$ **do**
  Set $\{u_h^{l,j+1}\} = \{u_h^{l,j}\}$
  for $l = 0$ *to* L **do** % cycle for direction
    Compute $S_d\left(\{u_h^{l,j+1}\}\right) = \sum_{i=0}^{L} w_i g(\boldsymbol{x}, \boldsymbol{\omega}_l \cdot \boldsymbol{\omega}_i) u_h^{i,j+1}$
    for $s = 1$ *to* S **do** % cycle for $T_h^{(l,s)}$
      Update $u_h^{l,j+1}$ on all elements K in $T_h^{(l,s)}$ by solving the problem (21)
    end for
  end for
  Compute $err = \left\|\{u_h^{l,j+1}\} - \{u_h^{l,j}\}\right\|_X$ Set $j = j + 1$
end while

4.2. Spatial cascadic multigrid method

For later presentation, we denote by the operator *RTEI* an iteration scheme for the numerical approximation of the RTE, that is,

$$\boldsymbol{u}_h = RTEI(T_h^X, T_{h_\theta}^\Omega, S_d^{h_\theta}, \boldsymbol{u}_h^0, M), \tag{24}$$

where T_h^X denotes the partition of X, $T_{h_\theta}^\Omega$ denotes the partition of Ω, $S_d^{h_\theta}$ represents the numerical approximation of the operator S with the parameter h_θ, $\boldsymbol{u}_h^0$ represents the initial value of the iteration scheme, and M stands for the number of iteration.

Let $T_0^X := T_{h_0}^X$ be an initial triangulation of X with mesh size h_0. Then we recursively generate a sequence of nested triangulations $T_j^X := T_{h_j}^X, j = 1, 2, \ldots, J$, by dividing each triangle in the previous mesh T_{j-1}^X into four sub-triangles by connecting the midpoints of the edges; $h_j = 2^{-j} h_0$.

Based on the operator *RTEI* and the meshes T_j^X, we describe the spatial cascadic multigrid method for the RTE in Algorithm 3.

Algorithm 3: Spatial cascadic multigrid method (*SCMG*)

For level $j = 0$: Let $\boldsymbol{u}_{h_0}^0$ be the DODSD approximation of RTE on T_0.
For level $j \geq 1$: Let $\boldsymbol{u}_{h_j}^0 = I_{j-1}^j \boldsymbol{u}_{h_{j-1}}^*$; compute $\boldsymbol{u}_{h_j}^* = RTEI(T_j^X, T_{h_\theta}^\Omega, S_d^{h_\theta}, \boldsymbol{u}_{h_j}^0, M_j)$.

Since the discrete spaces on $\{T_j\}$ are nested, the intergrid transfer operator I_{j-1}^j is the identity operator.

Following [42], we call a cascadic multigrid method optimal for level j (with respect to the weighted L^2 norm $\|\cdot\|_X$ of (18)) if

$$\|u_{h_j} - u_{h_j}^*\|_X \approx \|u - u_{h_j}\|_X, \tag{25}$$

meaning that the iteration error is comparable to the approximation error, and multigrid complexity

$$\text{amount of work} = O(N_j), \tag{26}$$

where N_j denotes the total number of unknowns associated with the partition $\{T_j\}$.

4.3. Analysis of complexity and accuracy

Letting N_j^K be the number of elements in T_j, we have $N_{j+1}^K = 2^d N_j^K$. If we apply the DODSD method with linear finite element space, then there are $(d+1)N_j^K$ unknowns for each direction with respect to T_j.

Use of the iteration defined earlier in the section implies that for each element, we need to solve a linear system of $d+1$ equations, which costs about $\frac{1}{3}(d+1)^3$ with the Gaussian elimination. Since there are N_j^K elements, the total computational cost of one iteration is $\frac{1}{3}(d+1)^3 N_j^K$ for each direction.

Assume that the number of iteration for level j satisfies

$$M_j \le M_J \beta^{J-j}, \quad \beta < 2^d. \tag{27}$$

Then the cascadic multigrid method is optimal in computational complexity.

Lemma 4.1. *If the assumption (27) holds, then the cascadic multigrid method is optimal in computational complexity, that is, the total computational cost for each direction is proportional to the number of unknowns with respect to T_J.*

Proof. By the definition of DODSD method, we know that the total number of unknowns for one direction with respect to the finest mesh T_J is $N_J = (d+1)N_J^K$.

On the other hand, the amount of computation for each direction is

$$\begin{aligned}
&M_1\left(\frac{1}{3}(d+1)^3 N_1^K\right) + M_2\left(\frac{1}{3}(d+1)^3 N_2^K\right) + \cdots + M_J\left(\frac{1}{3}(d+1)^3 N_J^K\right)\\
&= \frac{1}{3}(d+1)^3 (M_1 2^{(-J+1)d} + M_2 2^{(-J+2)d} + \cdots + M_J) N_J^K\\
&\le \frac{1}{3}(d+1)^3 \left(\left(\frac{\beta}{2^d}\right)^{J-1} + \left(\frac{\beta}{2^d}\right)^{J-2} + \cdots + 1\right) M_J N_J^K\\
&\le \frac{1}{3}(d+1)^2 \frac{2^d}{2^d - \beta} M_J N_J.
\end{aligned} \tag{28}$$

This implies that the total computational cost for solving the RTE is proportional to the number of unknowns of the J level, which completes the proof of this lemma. □

We comment that in our numerical experiments to be reported in Section 5, the condition (27) is satisfied with $\beta = 1$.

Next, we analyze the convergence property of the iteration scheme *RTEI*, which will be used as the smoother of the cascadic multigrid method.

In [54], a one-dimensional model for finite homogeneous medium problem

$$\mu \frac{\partial \Psi}{\partial x}(x,\mu) + \Sigma_t \Psi(x,\mu) = \frac{\Sigma_s}{2}\int_{-1}^{1} \Psi(x,\mu')\, d\mu' + \frac{Q(x)}{2}, \tag{29}$$

is used to quantitatively describe the performance of the SI scheme. The corresponding SI scheme is defined by

$$\mu \frac{\partial \Psi^{(k+1)}}{\partial x}(x,\mu) + \Sigma_t \Psi^{(k+1)}(x,\mu) = \frac{\Sigma_s}{2}\int_{-1}^{1} \Psi^{(k)}(x,\mu')\, d\mu' + \frac{Q(x)}{2}. \tag{30}$$

By the Fourier analysis, it was proved that

$$\left|\Psi(x,\mu) - \Psi^{(k)}(x,\mu)\right| \le Bc^k, \tag{31}$$

where $c = \frac{\Sigma_s}{\Sigma_t} < 1$ is the scattering ratio. We may replace the above inequality by

$$\left|\Psi(x,\mu) - \Psi^{(k+1)}(x,\mu)\right| \le c\left|\Psi(x,\mu) - \Psi^{(k)}(x,\mu)\right|. \tag{32}$$

For later analysis, we assume that the solution at each iteration for the discrete problem satisfies a similar relation:

$$\|u_h^{k+1} - u_h\|_X \le \Lambda \|u_h^k - u_h\|_X \tag{33}$$

with a constant $\Lambda \in (0,1)$ independent of h. In Section 5, some numerical examples are provided to illustrate the validity of the relation (33) for the source iteration and the Gauss–Seidel iteration.

We have the next result.

Lemma 4.2. *Assume (33) holds for the RTEI smoother. If the number of iterations M_j satisfies*

$$2^{\frac{3}{2}}\Lambda^{M_j} \le C_1, \quad j = 1, \ldots, J, \tag{34}$$

with some constant $C_1 \in (0, 1)$, then the cascadic multigrid method is optimal in accuracy, that is, the solution obtained by use of the cascadic multigrid method has the same convergence rate in $\|\cdot\|_X$ as the standard DODSD approximation on the finest mesh T_J.

Proof. Let $u^*_{h_j}$ and u_{h_j} be the solutions of the cascadic multigrid method and the DODSD method, respectively. It follows from (33) and Theorem 3.1 that

$$\begin{aligned}
\|u^*_{h_j} - u_{h_j}\|_X &= \|u^{M_j}_{h_j} - u_{h_j}\|_X \le \Lambda^{M_j}\|u^0_{h_j} - u_{h_j}\|_X \\
&\le \Lambda^{M_j}\|u^*_{h_{j-1}} - u_{h_j-1}\|_X + \Lambda^{M_j}\|u_{h_{j-1}} - u_{h_j}\|_X \\
&\le \Lambda^{M_j}\|u^*_{h_{j-1}} - u_{h_j-1}\|_X + C\Lambda^{M_j}\left(h_j^{\frac{3}{2}} + h_{j-1}^{\frac{3}{2}}\right)\left(\sum_{l=0}^{L}\|u^l\|^2_{r+1,X}\right)^{\frac{1}{2}} \\
&= \Lambda^{M_j}\|u^*_{h_{j-1}} - u_{h_j-1}\|_X + C\left(1 + 2^{\frac{3}{2}}\right)\Lambda^{M_j}h_j^{\frac{3}{2}}\left(\sum_{l=0}^{L}\|u^l\|^2_{r+1,X}\right)^{\frac{1}{2}}.
\end{aligned} \tag{35}$$

We apply (35) repeatedly,

$$\begin{aligned}
\|u^*_{h_J} - u_{h_J}\|_X &\le \Lambda^{M_J}\Lambda^{M_{J-1}}\|u^*_{h_{J-2}} - u_{h_J-2}\|_X \\
&\quad + C\left(1 + 2^{\frac{3}{2}}\right)\Lambda^{M_J}\Lambda^{M_{J-1}}h_{J-1}^{\frac{3}{2}}\left(\sum_{l=0}^{L}\|u^l\|^2_{r+1,X}\right)^{\frac{1}{2}} + C\left(1 + 2^{\frac{3}{2}}\right)\Lambda^{M_J}h_J^{\frac{3}{2}}\left(\sum_{l=0}^{L}\|u^l\|^2_{r+1,X}\right)^{\frac{1}{2}} \\
&= \Lambda^{M_J}\Lambda^{M_{J-1}}\|u^*_{h_{J-2}} - u_{h_J-2}\|_X + C\left(1 + 2^{\frac{3}{2}}\right)\left(\Lambda^{M_J}\Lambda^{M_{J-1}}h_{J-1}^{\frac{3}{2}} + \Lambda^{M_J}h_J^{\frac{3}{2}}\right)\left(\sum_{l=0}^{L}\|u^l\|^2_{r+1,X}\right)^{\frac{1}{2}}.
\end{aligned} \tag{36}$$

Processing in this way and noting that $u^*_{h_0} = u^0_{h_0}$, we have

$$\begin{aligned}
\|u^*_{h_J} - u_{h_J}\|_X &\le C\left(1 + 2^{\frac{3}{2}}\right)\left(\Lambda^{M_J}\Lambda^{M_{J-1}}\cdots\Lambda^{M_1}h_1^{\frac{3}{2}} + \cdots + \Lambda^{M_J}h_J^{\frac{3}{2}}\right)\left(\sum_{l=0}^{L}\|u^l\|^2_{r+1,X}\right)^{\frac{1}{2}} \\
&= C\left(1 + 2^{-\frac{3}{2}}\right)h_J^{\frac{3}{2}}\left(\Lambda^{M_J}2^{\frac{3}{2}}\Lambda^{M_{J-1}}2^{\frac{3}{2}}\cdots\Lambda^{M_1}2^{\frac{3}{2}} + \cdots + \Lambda^{M_J}2^{\frac{3}{2}}\right)\left(\sum_{l=0}^{L}\|u^l\|^2_{r+1,X}\right)^{\frac{1}{2}}.
\end{aligned} \tag{37}$$

Using the assumption (34), we get

$$\|u^*_{h_J} - u_{h_J}\|_X \le C\left(1 + 2^{-\frac{3}{2}}\right)h_J^{\frac{3}{2}}\left(C_1^J + C_1^{J-1}\cdots + C_1\right)\left(\sum_{l=0}^{L}\|u^l\|^2_{r+1,X}\right)^{\frac{1}{2}}.$$

Note that $C_1 \in (0, 1)$. Thus we get

$$\|u^*_{h_J} - u_{h_J}\|_X \le C\left(1 + 2^{-\frac{3}{2}}\right)h_J^{\frac{3}{2}}\min\left\{J, C_1(1 - C_1)^{-1}\right\}\left(\sum_{l=0}^{L}\|u^l\|^2_{r+1,X}\right)^{\frac{1}{2}}. \tag{38}$$

It follows from Theorem 3.1 that

$$\|u_{h_J} - u^l\|_X \le Ch_J^{\frac{3}{2}}\left(\sum_{l=0}^{L}\|u^l\|^2_{r+1,X}\right)^{\frac{1}{2}}. \tag{39}$$

Combining the above two inequalities, we obtain the stated result. □

From the above two lemmas, we deduce the following

Theorem 4.3. *Assume (33) holds for the RTEI smoother. If the number of iterations $M_j = M_J, \beta = 1, j = 1, \ldots, J$, and (34) holds, then the cascadic multigrid method is optimal in both accuracy and computational complexity.*

4.4. Full cascadic multigrid method

In the previous subsections, we proposed and analyzed the cascadic multigrid method only in the spatial variable, which uses the same angular partition for all levels. Now we consider the full cascadic multigrid method, which employs the cascadic multigrid method for both spatial and angular variables.

As in Section 4.3, let $T_j^X := T_j$ be a sequence of nested meshes for X with a mesh size $h_j, j = 1, 2, \ldots, J$. Let T_j^Ω be a sequence of partitions for Ω with mesh sizes $h_{\theta_j}, j = 1, 2, \ldots, J$. Thus for each level of the cascadic multigrid method, we have a partition T_j^X for the spatial variable and a partition T_j^Ω for the angular variable.

Since the discrete spaces $\{V_{h_j}\}$ on $\{T_j\}$ are nested, the interpolation operator from $V_{h_{j-1}}$ to V_{h_j} is the identity operator. As for the angular discretization, the numerical solution with respect to the direction ω_l on T_j^Ω may not have its counterpart at the last level, since T_{j-1}^Ω may not include the direction ω_l. Thus, we need to define the intergrid transfer operator I_{j-1}^j. For any direction $\omega_j^l \in T_j^\Omega$, let $\omega_{j-1}^p, \omega_{j-1}^q$ be the nearest directions to ω_j^l in T_{j-1}^Ω. Let $\boldsymbol{u}_{h_{j-1}}^p$ (and $\boldsymbol{u}_{h_{j-1}}^q$) be the numerical solution at level $j-1$ with respect to the direction ω_{j-1}^p (and ω_{j-1}^q). Then we define the part of $I_{j-1}^j \boldsymbol{u}_{h_{j-1}}$ associated with the direction ω_j^l to be the linear interpolation of $\boldsymbol{u}_{h_{j-1}}^p$ and $\boldsymbol{u}_{h_{j-1}}^q$.

Thus, the cascadic multigrid method in both space and angle for the RTE can be stated as in Algorithm 4.

Algorithm 4: Full cascadic multigrid method (*FCMG*)

For level $j = 0$: Let $\boldsymbol{u}_{h_0}^0$ be the DODSD approximation of RTE on T_0.

For level $j \geq 1$: Let $\boldsymbol{u}_{h_j}^0 = I_{j-1}^j \boldsymbol{u}_{h_{j-1}}^*$; compute $\boldsymbol{u}_{h_j}^* = RTEI(T_j^X, T_j^\Omega, S_d^{h_{\theta_j}}, \boldsymbol{u}_{h_j}^0, M_j)$.

Different from the spatial cascadic multigrid method, the intergrid transfer operator I_{j-1}^j in Algorithm 4 does not equal the identity operator, which will cause some additional interpolation error. As we shall see in the next section, the angular and spatial cascadic multigrid method needs some more smoothing iterations to reduce the error due to the interpolation.

5. Numerical experiments

In this section, we present some numerical examples to show the performance of the proposed cascadic multigrid methods for solving the radiative transfer equation (4)–(5).

Let the domain $X = (0, 1) \times (0, 1)$, and $T_0 = T_{h_0}$ be an initial triangulation of X with a mesh size $h_0 = 0.1$. Then we recursively generate nested triangulations $T_j = T_{h_j}, j = 1, 2, 3$, by dividing each triangle in the previous mesh T_{j-1} into four sub-triangles by connecting the midpoints of the edges. The linear element is employed on the spatial mesh with three refinements including 697, 2705, and 10 657 vertices, respectively.

Problem 1. Consider the RTE (4)–(5) with the Henyey–Greenstein phase function (3). The true solution is

$$u(\boldsymbol{x}, \boldsymbol{\omega}) = \sin(\pi x_1) \sin(\pi x_2).$$

We determine the right-hand side function $f(\boldsymbol{x}, \boldsymbol{\omega})$ from the radiative transfer equation. Corresponding to level j, we use $\delta = 10^{-5} h_j$.

Problem 2. Consider the RTE (4)–(5) with the phase function

$$g(\boldsymbol{x}, t) = \frac{1}{2\pi} \left(1 + \frac{t}{2}\right).$$

The true solution is

$$u(\boldsymbol{x}, \boldsymbol{\omega}) = e^{-ax_1 - bx_2} \left(1 + c \cos\theta\right),$$

with $a = b = \frac{\sigma_a}{3}$ and $c = \frac{\sigma_a}{\sigma_a + 6\sigma_s}$. We determine the right-hand side function $f(\boldsymbol{x}, \boldsymbol{\omega})$ from the radiative transfer equation. Corresponding to level j, we use $\delta = 10^{-5} h_j$.

5.1. Verification of the assumption (33)

The main purpose of this subsection is to illustrate the convergence performance of the source iteration scheme and the Gauss–Seidel iteration scheme.

First, we perform two tests on validity of the assumption (33) for the source iteration. For all numerical calculations, we consider the two model problems with $\sigma_t = 1.0, \sigma_s = 0.4$, and take $h_\theta = \frac{\pi}{10}$ for Problem 1.

Table 1
Error of SI scheme for Problem 1 with $\eta = 0.2$.

Iter. no.	$\|\boldsymbol{u}^*_{h_0} - \boldsymbol{u}_{h_0}\|_X$	Λ	$\|\boldsymbol{u}^*_{h_1} - \boldsymbol{u}_{h_1}\|_X$	Λ	$\|\boldsymbol{u}^*_{h_2} - \boldsymbol{u}_{h_2}\|_X$	Λ	$\|\boldsymbol{u}^*_{h_3} - \boldsymbol{u}_{h_3}\|_X$	Λ
1	2.0885e−01	–	2.0888e−01	–	2.0889e−01	–	2.0889e−01	–
2	2.7327e−02	0.13	2.7328e−02	0.13	2.7328e−02	0.13	2.7328e−02	0.13
3	3.5824e−03	0.13	3.5825e−03	0.13	3.5825e−03	0.13	3.5825e−03	0.13
4	4.7906e−04	0.13	4.7908e−04	0.13	4.7908e−04	0.13	4.7908e−04	0.13
5	6.4593e−05	0.13	6.4597e−05	0.13	6.4597e−05	0.13	6.4597e−05	0.13
6	8.7320e−06	0.14	8.7325e−06	0.14	8.7326e−06	0.14	8.7327e−06	0.14
7	1.1813e−06	0.14	1.1813e−06	0.14	1.1814e−06	0.14	1.1814e−06	0.14
8	1.5982e−07	0.14	1.5984e−07	0.14	1.5984e−07	0.14	1.5984e−07	0.14
9	2.1618e−08	0.14	2.1626e−08	0.14	2.1627e−08	0.14	2.1627e−08	0.14
10	2.9188e−09	0.14	2.9253e−09	0.14	2.9262e−09	0.14	2.9262e−09	0.14
11	3.8867e−10	0.13	3.9497e−10	0.14	3.9582e−10	0.14	3.9582e−10	0.14
12	4.6322e−11	0.12	5.2594e−11	0.13	5.3443e−11	0.14	5.3443e−11	0.14

Table 2
Error of SI scheme for Problem 2.

Iter. no.	$\|\boldsymbol{u}^*_{h_0} - \boldsymbol{u}_{h_0}\|_X$	Λ	$\|\boldsymbol{u}^*_{h_1} - \boldsymbol{u}_{h_1}\|_X$	Λ	$\|\boldsymbol{u}^*_{h_2} - \boldsymbol{u}_{h_2}\|_X$	Λ	$\|\boldsymbol{u}^*_{h_3} - \boldsymbol{u}_{h_3}\|_X$	Λ
1	3.2828e−01	–	3.2831e−01	–	3.2832e−01	–	3.2832e−01	–
2	4.8073e−02	0.15	4.8076e−02	0.15	4.8077e−02	0.15	4.8077e−02	0.15
3	6.9483e−03	0.14	6.9487e−03	0.14	6.9488e−03	0.14	6.9488e−03	0.14
4	9.9732e−04	0.14	9.9739e−04	0.14	9.9740e−04	0.14	9.9740e−04	0.14
5	1.4303e−04	0.14	1.4304e−04	0.14	1.4304e−04	0.14	1.4304e−04	0.14
6	2.0508e−05	0.14	2.0509e−05	0.14	2.0510e−05	0.14	2.0510e−05	0.14
7	2.9404e−06	0.14	2.9407e−06	0.14	2.9407e−06	0.14	2.9407e−06	0.14
8	4.2159e−07	0.14	4.2163e−07	0.14	4.2164e−07	0.14	4.2164e−07	0.14
9	6.0443e−08	0.14	6.0453e−08	0.14	6.0454e−08	0.14	6.0454e−08	0.14
10	8.6630e−09	0.14	8.6671e−09	0.14	8.6673e−09	0.14	8.6678e−09	0.14
11	1.2389e−09	0.14	1.2422e−09	0.14	1.2423e−09	0.14	1.2427e−09	0.14
12	1.7450e−10	0.14	1.7766e−10	0.14	1.7766e−10	0.14	1.7811e−10	0.14

Table 3
Error of GS scheme for Problem 1 with $\eta = 0.1$.

Iter. no.	$\|\boldsymbol{u}^*_{h_0} - \boldsymbol{u}_{h_0}\|_X$	Λ	$\|\boldsymbol{u}^*_{h_1} - \boldsymbol{u}_{h_1}\|_X$	Λ	$\|\boldsymbol{u}^*_{h_2} - \boldsymbol{u}_{h_2}\|_X$	Λ	$\|\boldsymbol{u}^*_{h_3} - \boldsymbol{u}_{h_3}\|_X$	Λ
1	1.8577e−01	–	1.8580e−01	–	1.8580e−01	–	1.8580e−01	–
2	1.6551e−02	0.09	1.6552e−02	0.09	1.6552e−02	0.09	1.6552e−02	0.09
3	1.2348e−03	0.07	1.2349e−03	0.07	1.2349e−03	0.07	1.2349e−03	0.07
4	8.5717e−05	0.07	8.5725e−05	0.07	8.5726e−05	0.07	8.5727e−05	0.07
5	5.8296e−06	0.07	5.8301e−06	0.07	5.8302e−06	0.07	5.8303e−06	0.07
6	3.9690e−07	0.07	3.9694e−07	0.07	3.9695e−07	0.07	3.9695e−07	0.07
7	2.7127e−08	0.07	2.7130e−08	0.07	2.7131e−08	0.07	2.7131e−08	0.07
8	1.8560e−09	0.07	1.8562e−09	0.07	1.8568e−09	0.07	1.8568e−09	0.07
9	1.2646e−10	0.07	1.2648e−10	0.07	1.2703e−10	0.07	1.2703e−10	0.07

For Problem 1, the convergence history of the source iteration scheme is reported in Table 1. From Table 1, we can see that: (1) the assumption (33) holds with a constant $\Lambda \approx 0.14$. (2) For the mesh on each level j, the source iterations have almost a same convergence rate. This implies that the convergence factor of the source iteration is not sensitive to h_j.

The results of the source iteration scheme for Problem 2 are reported in Table 2, which also confirm the validity of assumption (33).

The convergence history of the Gauss–Seidel iteration for solving Problems 1 and 2 is reported in Tables 3 and 4, which indicate that the assumption (33) also holds with $\Lambda \approx 0.09$ and $\Lambda \approx 0.06$ for these two examples respectively. Besides, we can see that for both problems the Gauss–Seidel iteration scheme offers a faster convergence rate than the source iteration scheme.

5.2. Spatial cascadic multigrid method

The main purpose of this subsection is to illustrate the accuracy of the proposed spatial cascadic multigrid method for the RTE. Since for both these examples, the Gauss–Seidel iteration scheme converges faster than the source iteration scheme, we only consider the spatial cascadic multigrid method with the Gauss–Seidel iteration smoother.

First, we consider Problems 1 and 2 with $\sigma_t = 1.0$ and $\sigma_s = 0.4$, and use the spatial cascadic multigrid method with the Gauss–Seidel smoother to solve these two problems on $T_{h_j}, j = 1, 2, 3$. The coarsest grid is T_{h_0}. The iteration number on each level j is one, i.e., $M_j = 1$ trivially. So the assumption (34) holds. By Theorem 4.3, the spatial cascadic multigrid method with the Gauss–Seidel iteration smoother is optimal in both accuracy and computational complexity. The numerical results are

Table 4
Error of GS scheme for Problem 2.

Iter. no.	$\|\boldsymbol{u}^*_{h_0} - \boldsymbol{u}_{h_0}\|_X$	Λ	$\|\boldsymbol{u}^*_{h_1} - \boldsymbol{u}_{h_1}\|_X$	Λ	$\|\boldsymbol{u}^*_{h_2} - \boldsymbol{u}_{h_2}\|_X$	Λ	$\|\boldsymbol{u}^*_{h_3} - \boldsymbol{u}_{h_3}\|_X$	Λ
1	2.1248e−01	–	2.1250e−01	–	2.1250e−01	–	2.1251e−01	–
2	1.3514e−02	0.06	1.3515e−02	0.06	1.3516e−02	0.06	1.3516e−02	0.06
3	6.8299e−04	0.05	6.8303e−04	0.05	6.8304e−04	0.05	6.8304e−04	0.05
4	3.1428e−05	0.05	3.1430e−05	0.05	3.1430e−05	0.05	3.1430e−05	0.05
5	1.4020e−06	0.04	1.4020e−06	0.04	1.4021e−06	0.04	1.4021e−06	0.04
6	6.2233e−08	0.04	6.2237e−08	0.04	6.2237e−08	0.04	6.2237e−08	0.04
7	2.7679e−09	0.04	2.7680e−09	0.04	2.7683e−09	0.04	2.7683e−09	0.04
8	1.2309e−10	0.04	1.2310e−10	0.04	1.2333e−10	0.04	1.2333e−10	0.04

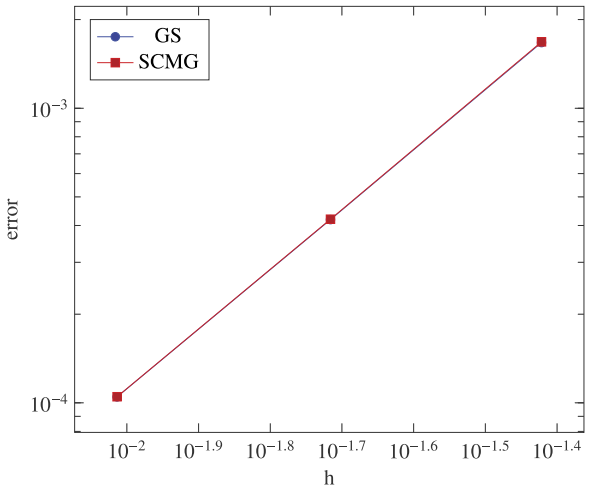

Fig. 3. Loglog convergence plot of $\|\boldsymbol{u} - \boldsymbol{u}_h\|_X$ for Problem 1 with $\eta = 0.2$. GS (blue) denotes the results by use of the Gauss–Seidel iteration without CMG. SCMG (red) denotes the results by use of the SCMG. (For interpretation of the references to color in this figure legend, the reader is referred to the web version of this article.)

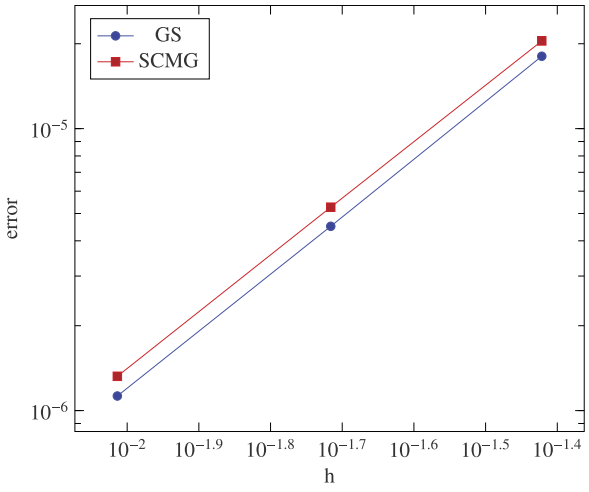

Fig. 4. Loglog convergence plot of $\|\boldsymbol{u} - \boldsymbol{u}_h\|_X$ for Problem 2. GS (blue) denotes the results by use of the Gauss–Seidel iteration without CMG. SCMG (red) denotes the results by use of the SCMG. (For interpretation of the references to color in this figure legend, the reader is referred to the web version of this article.)

shown in Figs. 3 and 4. From these figures, we observe that *SCMG* with one smoothing still keeps the optimal convergence rate in norm $\|\cdot\|_X$, which is the same as the convergence rate of the approximation solutions obtained by the Gauss–Seidel iteration.

Next, we consider the spatial cascadic multigrid method for Problem 1 with different parameters. From Tables 5–12, we can conclude that *SCMG* is optimal in accuracy.

Table 5
Convergence of *SCMG* for Problem 1 ($\sigma_t = 2.0, \sigma_s = 1.0$, $\eta = 0.3$, $h_\theta = \frac{\pi}{10}$).

M_j	$\|\boldsymbol{u}^*_{h_1} - \boldsymbol{u}\|_X$	$\|\boldsymbol{u}^*_{h_2} - \boldsymbol{u}\|_X$	$\|\boldsymbol{u}^*_{h_3} - \boldsymbol{u}\|_X$
1	1.6653e−03	4.1755e−04	1.0452e−04
2	1.6506e−03	4.1546e−04	1.0429e−04
3	1.6505e−03	4.1545e−04	1.0429e−04

Table 6
Convergence of *SCMG* for Problem 1 ($\sigma_t = 2.0, \sigma_s = 1.0$, $\eta = 0.6$, $h_\theta = \frac{\pi}{25}$).

M_j	$\|\boldsymbol{u}^*_{h_1} - \boldsymbol{u}\|_X$	$\|\boldsymbol{u}^*_{h_2} - \boldsymbol{u}\|_X$	$\|\boldsymbol{u}^*_{h_3} - \boldsymbol{u}\|_X$
1	1.6701e−03	4.1762e−04	1.0449e−04
2	1.6515e−03	4.1523e−04	1.0424e−04
3	1.6513e−03	4.1522e−04	1.0424e−04

Table 7
Convergence of *SCMG* for Problem 1 ($\sigma_s = 2.0, \sigma_s = 1.0$, $\eta = 0.9$, $h_\theta = \frac{\pi}{50}$).

M_j	$\|\boldsymbol{u}^*_{h_1} - \boldsymbol{u}\|_X$	$\|\boldsymbol{u}^*_{h_2} - \boldsymbol{u}\|_X$	$\|\boldsymbol{u}^*_{h_3} - \boldsymbol{u}\|_X$
1	1.6967e−03	4.2338e−04	1.0856e−04
2	1.6597e−03	4.1714e−04	1.0786e−04
3	1.6589e−03	4.1704e−04	1.0785e−04

Table 8
Convergence of *SCMG* for Problem 1 ($\sigma_t = 2.0, \sigma_s = 1.0$, $\eta = 0.99$, $h_\theta = \frac{\pi}{500}$).

M_j	$\|\boldsymbol{u}^*_{h_1} - \boldsymbol{u}\|_X$	$\|\boldsymbol{u}^*_{h_2} - \boldsymbol{u}\|_X$	$\|\boldsymbol{u}^*_{h_3} - \boldsymbol{u}\|_X$
1	1.7206e−03	4.3355e−04	1.1586e−04
2	1.6682e−03	4.2030e−04	1.1365e−04
3	1.6657e−03	4.1960e−04	1.1360e−04

Table 9
Convergence of *SCMG* for Problem 1 ($\sigma_t = 1.0, \sigma_s = 0.01, \eta = 0.3, h_\theta = \frac{\pi}{10}$).

M_j	$\|\boldsymbol{u}^*_{h_1} - \boldsymbol{u}\|_X$	$\|\boldsymbol{u}^*_{h_2} - \boldsymbol{u}\|_X$	$\|\boldsymbol{u}^*_{h_3} - \boldsymbol{u}\|_X$
1	1.6930e−03	4.2219e−04	1.0516e−04
2	1.6736e−03	4.1924e−04	1.0482e−04
3	1.6734e−03	4.1921e−04	1.0482e−04

Table 10
Convergence of *SCMG* for Problem 1 ($\sigma_t = 1.0, \sigma_s = 0.01, \eta = 0.6, h_\theta = \frac{\pi}{25}$).

M_j	$\|\boldsymbol{u}^*_{h_1} - \boldsymbol{u}\|_X$	$\|\boldsymbol{u}^*_{h_2} - \boldsymbol{u}\|_X$	$\|\boldsymbol{u}^*_{h_3} - \boldsymbol{u}\|_X$
1	1.6994e−03	4.2214e−04	1.0508e−04
2	1.6744e−03	4.1886e−04	1.0474e−04
3	1.6742e−03	4.1884e−04	1.0474e−04

Table 11
Convergence of *SCMG* for Problem 1 ($\sigma_t = 1.0, \sigma_s = 0.01, \eta = 0.9, h_\theta = \frac{\pi}{50}$).

M_j	$\|\boldsymbol{u}^*_{h_1} - \boldsymbol{u}\|_X$	$\|\boldsymbol{u}^*_{h_2} - \boldsymbol{u}\|_X$	$\|\boldsymbol{u}^*_{h_3} - \boldsymbol{u}\|_X$
1	1.7389e−03	4.3219e−04	1.1300e−04
2	1.6852e−03	4.2187e−04	1.1155e−04
3	1.6837e−03	4.2166e−04	1.1151e−04

Table 12
Convergence of *SCMG* for Problem 1 ($\sigma_t = 1.0$, $\sigma_s = 0.01$, $\eta = 0.99$, $h_\theta = \frac{\pi}{500}$).

M_j	$\|\boldsymbol{u}^*_{h_1} - \boldsymbol{u}\|_X$	$\|\boldsymbol{u}^*_{h_2} - \boldsymbol{u}\|_X$	$\|\boldsymbol{u}^*_{h_3} - \boldsymbol{u}\|_X$
1	1.7831e−03	4.5535e−04	1.2756e−04
2	1.7002e−03	4.2739e−04	1.2205e−04
3	1.6947e−03	4.2631e−04	1.2191e−04

Table 13
Convergence and computational time of *FCMG* for Problem 1 ($\sigma_t = 1.0$, $\sigma_s = 0.01$, $\eta = 0.9$, $h_\theta = \frac{\pi}{40}, \frac{\pi}{80}, \frac{\pi}{160}$, at level 1, 2, 3, respectively).

M_j	$\|\boldsymbol{u}^*_{h_1} - \boldsymbol{u}\|_X$	t	$\|\boldsymbol{u}^*_{h_2} - \boldsymbol{u}\|_X$	t	$\|\boldsymbol{u}^*_{h_3} - \boldsymbol{u}\|_X$	t
1	1.6678e−03	44.2	4.1797e−04	152.8	1.0461e−04	769.1
2	1.6675e−03	64.6	4.1793e−04	278.8	1.0460e−04	1480.1
3	1.6675e−03	87.3	4.1793e−04	409.7	1.0460e−04	2251.0

Table 14
Convergence and computational time of *SCMG* for Problem 1 ($\sigma_t = 1.0$, $\sigma_s = 0.01$, $\eta = 0.9$, $h_\theta = \frac{\pi}{160}, \frac{\pi}{160}, \frac{\pi}{160}$, at level 1, 2, 3, respectively).

M_j	$\|\boldsymbol{u}^*_{h_1} - \boldsymbol{u}\|_X$	t	$\|\boldsymbol{u}^*_{h_2} - \boldsymbol{u}\|_X$	t	$\|\boldsymbol{u}^*_{h_3} - \boldsymbol{u}\|_X$	t
1	1.6675e−03	258.3	4.1796e−04	486.0	1.0461e−04	1113.7
2	1.6672e−03	338.4	4.1792e−04	773.8	1.0460e−04	1972.2
3	1.6672e−03	432.5	4.1792e−04	1089.7	1.0460e−04	2934.4

Table 15
Convergence and computational time of *FCMG* for Problem 1 ($\sigma_t = 1.0$, $\sigma_s = 0.01$, $\eta = 0.95$, $h_\theta = \frac{\pi}{80}, \frac{\pi}{160}, \frac{\pi}{320}$, at level 1, 2, 3, respectively).

M_j	$\|\boldsymbol{u}^*_{h_1} - \boldsymbol{u}\|_X$	t	$\|\boldsymbol{u}^*_{h_2} - \boldsymbol{u}\|_X$	t	$\|\boldsymbol{u}^*_{h_3} - \boldsymbol{u}\|_X$	t
1	1.6676e−03	91.5	4.1798e−04	327.0	1.0461e−04	1611.7
2	1.6673e−03	138.2	4.1793e−04	596.7	1.0460e−04	3098.2
3	1.6673e−03	163.5	4.1793e−04	767.6	1.0460e−04	4308.3

Table 16
Convergence and computational time of *SCMG* for Problem 1 ($\sigma_t = 1.0$, $\sigma_s = 0.01$, $\eta = 0.95$, $h_\theta = \frac{\pi}{320}, \frac{\pi}{320}, \frac{\pi}{320}$, at level 1, 2, 3, respectively).

M_j	$\|\boldsymbol{u}^*_{h_1} - \boldsymbol{u}\|_X$	t	$\|\boldsymbol{u}^*_{h_2} - \boldsymbol{u}\|_X$	t	$\|\boldsymbol{u}^*_{h_3} - \boldsymbol{u}\|_X$	t
1	1.6676e−03	465.1	4.1797e−04	876.6	1.0461e−04	2001.6
2	1.6673e−03	633.2	4.1792e−04	1448.7	1.0460e−04	3675.1
3	1.6673e−03	800.9	4.1792e−04	2022.4	1.0460e−04	5349.8

5.3. Full cascadic multigrid method

In this section, we employ the full cascadic multigrid method described in Section 4.4 to solve Problems 1 and 2. We take $\sigma_t = 1.0$, $\sigma_s = 0.01$ for Problem 1, and $\sigma_t = 1.0$, $\sigma_s = 0.4$ for Problem 2. The Gauss–Seidel iteration smoother is employed in all the following examples. The numerical results are reported in Tables 13–18. For comparison, the results by use of the *SCMG* and the conventional Gauss–Seidel iteration scheme with the finest mesh are also included. The computational time (t) has unit second.

From Tables 13–18, we can conclude that the full cascadic multigrid method with different iteration numbers preserves the same optimal convergence rate in $\|\cdot\|_X$ as in the spatial cascadic multigrid method. Another conclusion is that, generally, one, or at most two iterations at each level provides sufficient accuracy. It can also be observed that the result in Lemma 4.1 holds not only for *SCMG* but also for *FCMG*, i.e., the computational costs for *SCMG* and *FCMG* are approximately proportional to the number of unknowns with respect to both angular and spatial meshes. Thus these two multigrid methods are optimal for these examples.

The comparison of the errors and computational times generated by use of *FCMG*, *SCMG*, and the conventional Gauss–Seidel iteration scheme are reported in Tables 19–21. These results indicate that *FCMG* can accelerate the computation significantly. Furthermore, the proposed cascadic multigrid methods are effective for highly forward-peaked cases.

Table 17
Convergence and computational time of *FCMG* for Problem 2 ($\sigma_t = 1.0$, $\sigma_s = 0.4$, $h_\theta = \frac{\pi}{10}, \frac{\pi}{20}, \frac{\pi}{40}$, at level 1, 2, 3, respectively).

M_j	$\|\boldsymbol{u}^*_{h_1} - \boldsymbol{u}\|_X$	t	$\|\boldsymbol{u}^*_{h_2} - \boldsymbol{u}\|_X$	t	$\|\boldsymbol{u}^*_{h_3} - \boldsymbol{u}\|_X$	t
1	2.3806e−04	16.6	5.6945e−05	46.7	1.3579e−05	212.9
2	1.6767e−05	22.9	4.1551e−06	82.8	1.0375e−06	411.3
3	1.7820e−05	29.8	4.4605e−06	124.8	1.1164e−06	667.2

Table 18
Convergence and computational time of *SCMG* for Problem 2 ($\sigma_t = 1.0$, $\sigma_s = 0.4$, $h_\theta = \frac{\pi}{40}, \frac{\pi}{40}, \frac{\pi}{40}$, at level 1, 2, 3, respectively).

M_j	$\|\boldsymbol{u}^*_{h_1} - \boldsymbol{u}\|_X$	t	$\|\boldsymbol{u}^*_{h_2} - \boldsymbol{u}\|_X$	t	$\|\boldsymbol{u}^*_{h_3} - \boldsymbol{u}\|_X$	t
1	2.0392e−05	101.7	5.2337e−06	163.7	1.3143e−06	322.4
2	1.8136e−05	136.3	4.5365e−06	258.9	1.1347e−06	595.2
3	1.8030e−05	156.1	4.5099e−06	346.9	1.1281e−06	865.5

Table 19
Comparison of the computational time for the *FCMG* ($M_j = 1$), *SCMG* ($M_j = 1$), and the Gauss–Seidel (*GS*) iteration without CMG for Problem 1 ($\sigma_t = 1.0$, $\sigma_s = 0.01$, $\eta = 0.9$, $h_\theta = \frac{\pi}{160}$).

Method	$\|\boldsymbol{u}^*_{h_3} - \boldsymbol{u}\|_X$	t
FCMG	1.0461e−04	769.1
SCMG	1.0461e−04	1113.7
GS	1.0460e−04	2455.4

Table 20
Comparison of the computational time for the *FCMG* ($M_j = 5$ and 55 iterations at the coarsest grid to reach the accuracy set by the tolerance 10^{-4}), *SCMG* ($M_j = 5$ and 55 iterations at the coarsest grid to reach the accuracy set by the tolerance 10^{-4}), and the *GS* scheme (76 iterations) without CMG for Problem 1. ($\sigma_t = 100.0$, $\sigma_s = 90.0$, $\eta = 0.9$, $h_\theta = \frac{\pi}{64}, \frac{\pi}{128}, \frac{\pi}{256}$ for FCMG, and $h_\theta = \frac{\pi}{256}$ for SCMG and GS).

Method	$\|\boldsymbol{u}^*_{h_2} - \boldsymbol{u}\|_X$	t
FCMG	3.8320e−04	3905.3
SCMG	3.8377e−04	7370.7
GS	3.7906e−04	26361.6

Table 21
Comparison of the computational time for the *FCMG* ($M_j = 3$), *SCMG* ($M_j = 3$), and the Gauss–Seidel (*GS*) iteration without CMG for Problem 2 ($\sigma_t = 1.0$, $\sigma_s = 0.4$, $h_\theta = \frac{\pi}{40}$).

Method	$\|\boldsymbol{u}^*_{h_3} - \boldsymbol{u}\|_X$	t
FCMG	1.1164e−06	667.2
SCMG	1.1281e−06	865.5
GS	1.1277e−06	1173.8

5.4. Comparison with the conventional MG methods

In this subsection, we present some numerical results about the comparison between the CMG and conventional MG methods. Here the conventional MG methods are referred to the MG1, MG2, MG3 and MG4 methods proposed in [41]. Note that one needs to solve the elemental subproblem (22) on each element in one smoothing step for the CMG method and needs to solve the elemental subproblem (27) of [41] for the conventional MG methods. Since both elemental subproblems are 3×3 linear systems, the computational costs for solving these elemental subproblems are nearly identical. Therefore, we measure the computational cost in terms of the number of such linear systems involved for comparison.

We consider the settings of Problem 1, and take $\sigma_t = 100$, $\sigma_s = 10$, and $\eta = 0.9$. The spatial meshes have 328, 1312, 5248 triangular elements at level 1, 2, and 3, respectively. The angular partitions have 128, 256, and 512 nodes at level 1, 2, and 3, respectively. We use the term level (i, j) to represent the combination of angular level i and spatial level j.

To solve this problem, the CMG method takes 55 iterations at level (1, 1), 5 iterations at level (2, 2), and 5 iterations at level (3, 3). Totally, the number of 3-by-3 linear systems involved is

$$328 \times 128 \times 55 + 256 \times 1312 \times 5 + 512 \times 5248 \times 5 = 17\,423\,360,$$

Table 22
Comparison between the CMG and conventional MG methods.

Method	$\|\boldsymbol{u}_h^* - \boldsymbol{u}\|_X$	Computational cost
CMG	3.5e−3	17 423 360
MG1	7.1e−3	56 006 656
MG2	7.1e−3	55 838 720
MG3	7.1e−3	39 380 992
MG4	7.0e−3	41 984 000

which represents the computational cost for the CMG method. As for the conventional MG methods, we use the codes by the authors of the Ref. [41], available from the public domain (https://sites.google.com/site/rtefastsolver/). The MG4 method takes 16 iterations at level (1, 1), 14 iterations at level (1, 2), 12 iterations at level (2, 2), 10 iterations at level (2, 3), and 8 iterations at level (3, 3). Hence the computational cost of the MG4 method is

$$328 \times 128 \times 16 + 128 \times 1312 \times 14 + 256 \times 1312 \times 12 + 256 \times 5248 \times 10 + 512 \times 5248 \times 8 = 41984000.$$

The computational costs of other conventional MG methods are calculated in the same way. All these results, together with the errors in $\|\cdot\|_X$ norm, are reported in Table 22.

From this table, we observe that the computational cost of the CMG method is less than the conventional MG methods. We remark that the discrete-ordinate discontinuous-streamline diffusion scheme is employed in our algorithm while the discrete-ordinate discontinuous Galerkin method is employed in the conventional MG methods. This difference is the reason why the CMG method is more accurate than the conventional MG method for this example.

6. Conclusion

In this paper, we develop two cascadic multigrid methods for solving the RTE which use an iteration scheme satisfying the assumption (33) as the smoother, and take the iteration number satisfying the condition (34) on each level. Our numerical experiments show that both the proposed CMG methods are optimal in accuracy and computational complexity, and the ASCMG method achieves a faster convergence in comparison with the SCMG method since the cascadic multigrid algorithm is applied to both spatial and angular variables in the ASCMG method.

While the investigations of basic aspects of the cascadic multigrid method in this paper indicate the method is promising in solving the RTE, there is much to be done in the future, including estimating the convergence factor Λ, selecting the best smoother, designing a more efficient stopping condition other than (34), and constructing the interpolation operator for different angular partitions.

Acknowledgments

We thank the reviewers for their valuable comments and suggestions.

References

[1] A. Peraiah, An Introduction to Radiative Transfer: Methods and Applications in Astrophysics, Cambridge University Press, 2001.
[2] J.A. Coakley Jr., P. Yang, Atmospheric Radiation: A Primer with Illustrative Solutions, Wiley-VCH Verlag, Germany, 2014.
[3] G.E. Thomas, K. Stamnes, Radiative Transfer in the Atmosphere and Ocean, Cambridge University Press, 1999, http://dx.doi.org/10.1017/CBO9780511613470.
[4] W. Zdunkowski, T. Trautmann, A. Bott, Radiation in the Atmosphere: A Course in Theoretical Meteorology, Cambridge University Press, 2007.
[5] M.F. Modest, Radiative Heat Transfer, third ed., Academic Press, 2013.
[6] K.M. Case, P.F. Zweifel, Linear Transport Theory, Addison-Wesley, Reading, MA, 1967.
[7] J.J. Duderstadt, W.R. Martin, Transport Theory, John Wiley, New York, 1978.
[8] Y. Azmy, E. Sartori (Eds.), Nuclear Computational Science: A Century in Review, Springer, New York, 2010.
[9] D.G. Cacuci (Ed.), Handbook of Nuclear Engineering, Springer, New York, 2010.
[10] H. Hensel, R. Iza-Teran, N. Siedow, Deterministic model for dose calculation in photon radiotherapy, Phys. Med. Biol. 51 (3) (2006) 675.
[11] D.M.J. Lovelock, C.S. Chui, R. Mohan, A Monte Carlo model of photon beams used in radiation therapy, Med. Phys. 22 (9) (1995) 1387–1394. http://dx.doi.org/10.1118/1.597620.
[12] F. Natterer, F. Wübbeling, Mathematical Methods in Image Reconstruction, Society for Industrial and Applied Mathematics, 2001, http://dx.doi.org/10.1137/1.9780898718324.
[13] S.R. Arridge, Optical tomography in medical imaging, Inverse Problems 15 (2) (1999) R41. URL: http://stacks.iop.org/0266-5611/15/i=2/a=022.
[14] S.R. Arridge, J.C. Schotland, Optical tomography: forward and inverse problems, Inverse Problems 25 (12) (2009) 123010. URL: http://stacks.iop.org/0266-5611/25/i=12/a=123010.
[15] G. Bal, Inverse transport theory and applications, Inverse Problems 25 (5) (2009) 053001. URL: http://stacks.iop.org/0266-5611/25/i=5/a=053001.
[16] W. Han, J. Eichholz, X. Cheng, G. Wang, A theoretical framework of X-ray dark-field tomography, SIAM J. Appl. Math. 71 (5) (2011) 1557–1577. http://dx.doi.org/10.1137/100809039.
[17] K. Ren, Recent developments in numerical techniques for transport-based medical imaging methods, Commun. Comput. Phys. 8 (2010) 1–50. http://dx.doi.org/10.4208/cicp.220509.200110a.
[18] J. Tang, W. Han, B. Han, A theoretical study for RTE-based parameter identification problems, Inverse Problems 29 (9) (2013) 095002. URL: http://stacks.iop.org/0266-5611/29/i=9/a=095002.
[19] P. González-Rodríguez, A.D. Kim, Light propagation in tissues with forward-peaked and large-angle scattering, Appl. Opt. 47 (14) (2008) 2599–2609. http://dx.doi.org/10.1364/AO.47.002599.

[20] P. Bloch, M. Altschuler, Three-dimensional photon beam calculations, in: A. Smith (Ed.), Radiation Therapy Physics, Medical Radiology, Springer, Berlin, Heidelberg, 1995, pp. 33–42. http://dx.doi.org/10.1007/978-3-662-03107-0_3.
[21] J.A. Fleck Jr., J.D. Cummings Jr., An implicit Monte Carlo scheme for calculating time and frequency dependent nonlinear radiation transport, J. Comput. Phys. 8 (3) (1971) 313–342. http://dx.doi.org/10.1016/0021-9991(71)90015-5.
[22] J.R. Howell, The Monte Carlo method in radiative heat transfer, J. Heat Transfer 120 (3) (1998) 547–560. http://dx.doi.org/10.1115/1.2824310.
[23] I. Lux, L. Koblinger, Monte Carlo Particle Transport Methods: Neutron and Photon Calculations, CRC Press, 1991.
[24] J. Spanier, E. Gelbard, Monte Carlo Principles and Neutron Transport Problems, Dover, New York, 2008.
[25] E.E. Lewis, W.F. Miller, Computational Methods of Neutron Transport, John Wiley & Sons, New York, 1984.
[26] W.R. Martin, C.E. Yehnert, L. Lorence, J.J. Duderstad, Phase-space finite element methods applied to the first-order form of the transport equation, Ann. Nucl. Energy 8 (1981) 633–646. http://dx.doi.org/10.1016/0306-4549(81)90131-6.
[27] W. Han, J. Huang, J. Eichholz, Discrete-ordinate discontinuous Galerkin methods for solving the radiative transfer equation, SIAM J. Sci. Comput. 32 (2) (2010) 477–497. http://dx.doi.org/10.1137/090767340.
[28] G.D. Raithby, E.H. Chui, A finite-volume method for predicting a radiant heat transfer in enclosures with participating media, J. Heat Transfer 112 (2) (1990) 415–423. http://dx.doi.org/10.1115/1.2910394.
[29] R. Koch, W. Krebs, S. Wittig, R. Viskanta, Discrete ordinates quadrature schemes for multidimensional radiative transfer, J. Quant. Spectrosc. Radiat. Transfer 53 (4) (1995) 353–372. http://dx.doi.org/10.1016/0022-4073(95)90012-8.
[30] B.G. Carlson, K.D. Lathrop, Transport theory: The method of discrete ordinates, in: H. Greenspan, C.N. Kelber, D. Okrent (Eds.), Computing Methods in Reactor Physics, Gordon and Breach Science Publishers, New York, 1968, pp. 171–266.
[31] H. Egger, M. Schlottbom, A mixed variational framework for the radiative transfer equation, Math. Models Methods Appl. Sci. 22 (03) (2012) 1150014. http://dx.doi.org/10.1142/S021820251150014X.
[32] H. Gao, H. Zhao, Analysis of a numerical solver for radiative transport equation, Math. Comp. 82 (281) (2013) 153–172 http://dx.doi.org/10.1090/S0025-5718-2012-02605-6.
[33] R.G. McClarren, C.D. Hauck, Simulating radiative transfer with filtered spherical harmonics, Phys. Lett. A 374 (22) (2010) 2290–2296 http://dx.doi.org/10.1016/j.physleta.2010.02.041.
[34] W. Han, J. Eichholz, Q. Sheng, Theory of differential approximations of radiative transfer equation, in: Advances in Applied Mathematics and Approximation Theory, Springer, 2013, pp. 121–148. http://dx.doi.org/10.1007/978-1-4614-6393-1_8.
[35] W. Han, Y. Li, Q. Sheng, J. Tang, A numerical method for generalized Fokker–Planck equations, in: Contemporary Mathematics, Vol. 586, American Mathematical Society, 2013, pp. 171–179. http://dx.doi.org/10.1090/conm/586/11649.
[36] J.H. Ferziger, M. Peric, Computational Methods for Fluid Dynamics, third ed., Springer-Verlag, Berlin, Heidelberg, 2002, http://dx.doi.org/10.1007/978-3-642-56026-2.
[37] J. Blazek, Computational Fluid Dynamics: Principles and Applications, second ed., Elsevier Science, 2006.
[38] D. Balsara, Fast and accurate discrete ordinates methods for multidimensional radiative transfer. Part I, basic methods, J. Quant. Spectrosc. Radiat. Transfer 69 (6) (2001) 671–707. http://dx.doi.org/10.1016/S0022-4073(00)00114-X.
[39] G.N. Lygidakis, I.K. Nikolos, Using a parallel spatial/angular agglomeration multigrid scheme to accelerate the FVM radiative heat transfer computation–Part I: Methodology, Numer. Heat Transf. Part B: Fundam. 66 (6) (2014) 471–497. http://dx.doi.org/10.1080/10407790.2014.949561.
[40] G.N. Lygidakis, I.K. Nikolos, Using a parallel spatial/angular agglomeration multigrid scheme to accelerate the FVM radiative heat transfer computation–Part II: Numerical results, Numer. Heat Transf. Part B: Fundam. 66 (6) (2014) 498–525. http://dx.doi.org/10.1080/10407790.2014.949509.
[41] H. Gao, H. Zhao, A fast-forward solver of radiative transfer equation, Transport Theory Statist. Phys. 38 (3) (2009) 149–192 http://dx.doi.org/10.1080/00411450903187722.
[42] F.A. Bornemann, P. Deuflhard, The cascadic multigrid method for elliptic problems, Numer. Math. 75 (1996) 135–152 http://dx.doi.org/10.1007/s002110050234.
[43] D. Braess, W. Dahmen, A cascadic multigrid algorithm for the Stokes equations, Numer. Math. 82 (2) (1999) 179–191.
[44] Z.-C. Shi, X.-J. Xu, A cascadic multigrid, Sci. China Ser. A Math. 44 (2001) 21–30.
[45] D. Braess, P. Deuflhard, K. Lipnikov, A subspace cascadic multigrid method for mortar elements, Computing 69 (3) (2002) 205–225.
[46] Z.-C. Shi, X.-J. Xu, Y.-Q. Huang, Economical cascadic multigrid method (ECMG), Sci. China Ser. A 50 (12) (2007) 1765–1780.
[47] Q. Du, P. Ming, Cascadic multigrid methods for parabolic problems, Sci. China Ser. A 51 (8) (2008) 1415–1439.
[48] C. Wang, Q. Sheng, W. Han, A discrete-ordinate discontinuous-streamline diffusion method for the radiative transfer equation, submitted for publication, 2015 http://arxiv.org/abs/1603.03356.
[49] L. Henyey, J. Greenstein, Diffuse radiation in the galaxy, Astrophys. J. 93 (1941) 70–83.
[50] V. Agoshkov, Boundary Value Problems for Transport Equations, Birkhäuser, Boston, 1998.
[51] K. Atkinson, An Introduction to Numerical Analysis, second ed., John Wiley & Sons, New York, 1989.
[52] K. Hesse, I.H. Sloan, Cubature over the sphere S^2 in Sobolev spaces of arbitrary order, J. Approx. Theory 141 (2) (2006) 118–133 http://dx.doi.org/10.1016/j.jat.2006.01.004.
[53] E.E. Lewis, J. Warren, F. Miller, Computational Methods of Neutron Transport, American Nuclear Society, 1993.
[54] M.L. Adams, E.W. Larsen, Fast iterative methods for discrete-ordinates particle transport calculations, Prog. Nucl. Energy 40 (2002) 3–159. http://dx.doi.org/10.1016/S0149-1970(01)00023-3.